Research Square

Preprints are preliminary reports that have not undergone peer review.
They should not be considered conclusive, used to inform clinical practice,
or referenced by the media as validated information.

MXene/Polypyrrole/NiO Hybrid Nanostructure for Efficient Supercapacitor Energy Storage Applications

Muhammad Gohar
University of Southern Punjab
Muhammad Ismail
Universiti Malaysia Sabah
Mariyam Asif
Forman Christian College (A Chartered University)
Mohamad Zul Hilmey Makmud
Universiti Malaysia Sabah
YanYan Farm
yanyan@ums.edu.my
Universiti Malaysia Sabah
Mohammad Waseem
Bahuddin Zakariya University

Research Article

Keywords: MXene, polypyrrole, nickel oxide, Ti3C2Tx, ternary nanocomposite, supercapacitor, pseudocapacitance, energy storage

Posted Date: November 26th, 2026

DOI: https://doi.org/10.21203/rs.3.rs-11424424/v1

License: This work is licensed under a Creative Commons Attribution 4.0 International License.
Read Full License

Additional Declarations: No competing interests reported.

MXene/Polypyrrole/NiO Hybrid Nanostructure for Efficient Supercapacitor Energy Storage Applications

Muhammad Gohar[1], Muhammad Ismail[2], Mariyam Asif[3], Mohamad Zul Hilmey Makmud[2], YanYan Farm[2,4]*, Mohammad Waseem[5]

[1]Department of Chemistry, University of Southern Punjab, Multan, Punjab, 60750, Pakistan.

[2]Energy Laboratory, Green Technologies and Advanced Matter (GREAT) Research Group, Faculty of Science and Technology, Universiti Malaysia Sabah, Kota Kinabalu, Sabah 88400, Malaysia

[3]Department of Chemistry Forman Christian College (A Chartered University), Lahore

[4]Department of Mechanical, Faculty of Engineering, Universiti Malaysia Sabah, Kota Kinabalu, Sabah 88400, Malaysia

[5]Institute of Chemical Sciences, Bahuddin Zakariya University Multan, Pakistan

Croospounding author

Email: yanyan@ums.edu.my

Abstract

The $Ti_3C_2T_x$ MXene/Polypyrrole@Nickel oxide (MXene/PPy@NiO) nanocomposite was successfully fabricated using a fluoride-free Potassium hydroxide (KOH)-assisted hydrothermal etching process, in-situ oxidative polymerization of pyrrole, and the hydrothermal deposition of Nickel oxide (NiO). MXene with the incorporation of PPy and NiO has larger interlayer spacing, partially restricts the restacking of the MXene sheets, and promotes electrical conductivity and structural stability during electrochemical cycling. The optimized ternary hybrid possesses a large pore volume of 0.54 cm^3g^{-1} and a large BET surface area of 74.28 m^2g^{-1}. The material showed a remarkable specific capacitance of 517 F g^{-1} under galvanostatic charge-discharge (GCD) conditions with a current load of 1 A g^{-1} for a three-electrode system in 1 M KOH aqueous electrolyte. The specific capacitance of 421 F g^{-1} was obtained by cyclic voltammetry (CV) at 5 mV s^{-1} scan rate. Impedance spectroscopy revealed the charge-transfer resistance (Rct) to be ~1.8 Ω, while the capacitance of the three-electrode system did not drop by more than 82% after 2000 charge-discharge cycles. A two-electrode asymmetric MXene/PPy@NiO supercapacitor was then fabricated, which exhibited a specific capacitance of 180 F g^{-1}, a maximum energy density of 64 Wh kg^{-1}, a power density of 640 W kg^{-1}, and still had 88% of its capacitance after 5000 charge–discharge cycles, and could be used to light a commercial red LED under laboratory conditions. The improved electrochemical activities show the potential of MXene/polymer/metal oxide composites as promising electrode materials for advanced supercapacitor applications.

Graphical abstract

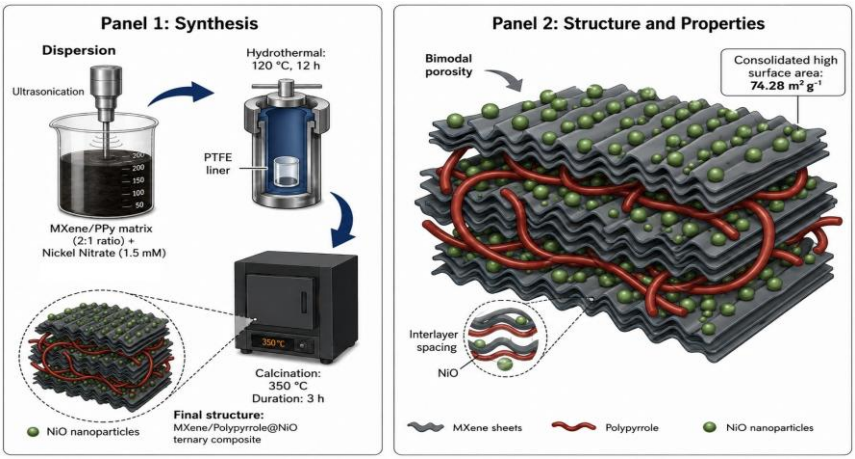

Keywords: MXene; polypyrrole; nickel oxide; $Ti_3C_2T_x$; ternary nanocomposite; supercapacitor; pseudocapacitance; energy storage

1. Introduction

There is a high demand for energy storage devices that provide a rapid charge and discharge capability combined with high power output and extended operational life [1]. Electrochemical supercapacitors are a promising technology effectively filling the performance void between standard dielectric capacitors and secondary batteries [2]. Batteries are extremely slow in transporting energy despite storing a considerable amount of energy [3], while Supercapacitors have relatively low energy storage capacity, yet they have high power density [4]. Thus, recent studies focus on the charge storage mechanisms in a supercapacitor through electric double-layer capacitance, surface-bound faradaic pseudocapacitance, or a combination of both mechanisms [5]. Thus, such a rational electrode design is required, combining a conductive backbone, an accessible surface area, stable interfaces, and redox activity.

MXenes represent an emerging class of metal carbides, nitrides, or carbonitrides [6]. $Ti_3C_2T_x$ is one of the most studied MXenes used in advanced energy storage applications due to the presence of conductive layers that enable electron transport and ion-accessible surfaces [7]. Typically, a conventional method to produce MXenes involves etching the Al layers with HF or a mixture of LiF/HCl, a process that is efficient and effective but generates surface terminations containing fluorine and poses serious handling risks. In this work, a KOH-assisted method is used to synthesize MXene $Ti_3C_2T_x$, a route with no fluoride, and it is capable of selective leaching of aluminum under controlled conditions, minimizing environmental and safety issues.[8]. However, the electrochemical utilization of pristine MXenes is often lower than desired due to the nanosheet restacking during drying and electrode fabrication, which reduces the available surface area and decreases ion mobility [9]. While no direct comparison was done with the conventionally HF-etched MXene, the goal of the present work was to explore the viability of a KOH-assisted process to develop electrochemically active MXene composites without the use of fluorine.

Over the last few years, a few ternary composites made up of combinations of polymers and metal oxides based on the MXenes have been reported [10]. In comparison, this current work of MXene/PPy@NiO composite achieves better performance with the sequential synthesis of $Ti_3C_2T_x$ using KOH, in-situ polymerization of PPy, and hydrothermal deposition of NiO. The limitations and a clear gap in the literature for high-performance ternary supercapacitor electrodes are minimized in this study [11]. Conducting polymers such as PPy improve the electrical conductivity and pseudocapacitance performance of MXene electrodes by reducing the tendency for sheet restacking while facilitating electrolyte penetration and charge transport [12]. Similarly, NiO contributes high faradaic capacitance through reversible Ni^{2+}/Ni^{3+} redox reactions, while its poor conductivity and agglomeration can be effectively overcome by integrating it with MXenes and conducting polymers [13]. This blend should yield a higher capacitance, charge-transfer kinetics, and electrolyte access than when used alone or in binary blends [14]. In the present manuscript, the synthesis, structural characterization, textural analysis, and electrochemical evaluation of MXene/PPy@NiO as a supercapacitor electrode material have been reported.

2. Materials and Methods

2.1 Chemical reagents

The Chemical precursors and analytical grade reagents such as titanium aluminum carbide (Ti_3AlC_2), potassium hydroxide (KOH), nickel(II) nitrate hexahydrate [$Ni(NO_3)_2{\cdot}6H_2O$] and ammonium persulfate (APS), pyrrole monomer, polyvinylidene fluoride (PVDF), hydrochloric acid (HCl), ethanol, N-methyl-2-pyrrolidone (NMP), and deionized water were used for synthesis and electrode preparation.

2.2 Preparation of $Ti_3C_2T_x$ MXene for Electrochemical Applications

The hydrothermal etching process based on KOH was carried out with a few modifications as reported in another study [15] to synthesize $Ti_3C_2T_x$ MXene. Briefly, the synthesis was performed by adding 0.30 g of KOH, 0.10 g of Ti_3AlC_2, and 0.05 mL of deionized water to an agate mortar and mixing until a uniform paste was formed. The prepared paste was placed in the 50 mL PTFE-lined autoclave, and after autoclaving for 24 h at 180 °C, it was removed. After reaching room temperature, the product was centrifuged (8000 rpm) for 10 min and washed many times with deionized water to get the neutral pH. The product was then vacuum-dried at 60 °C for a period of 12 h to yield $Ti_3C_2T_x$ MXene nanosheets. In the preliminary experiments, the reaction time was optimized to successfully extract Al with very little oxidation of the Ti3C2 frameworks, and also the concentration of KOH and the hydrothermal temperature were optimized.. Throughout the study, these conditions were kept the same to guarantee reproducible synthesis. The hydroxide ions in hydrothermal treatment selectively replace the Al layers in Ti_3AlC_2 to form soluble potassium aluminate species, thereby selectively extracting Al and exposing the layered $Ti_3C_2T_x$ structure. The optimized reaction conditions reduced the amount of excess oxidation of titanium, which affected the layered structure, crucial for electrochemical applications. The aim of the study was the electrochemical characterization of the obtained MXene and not the optimization of process-scale production, so the synthesis was optimized for the structural quality of the obtained product, as well as for its electrochemical properties.

2.3 Preparation of MXene/PPy Composite

The reported procedure for synthesizing the MXene/PPy composite was via in situ oxidative polymerization with slight modifications [16]. The prepared MXene (50mg) was dispersed in 50mL of 0.1 M HCl containing 0.1 M pyrrole monomer by sonication for 30 min to yield a homogeneous sample. The reaction mixture was maintained at 0–5 °C using an ice-water bath to control the polymerization rate of the growing PPy chains. Subsequently, a 0.1 M APS solution prepared in 10mL of 0.1 M HCl was added dropwise over 30 min under vigorous stirring. The polymerization proceeded at 0-5 °C for a duration of 6 h. The low polymerization temperature and the dropwise addition of APS suppressed the over-oxidation of MXene sheets to ensure uniform growth of PPy on their surface. The precipitate was then collected by centrifugation, rinsed with DI water to remove the monomers, and then dried in an oven at 60 °C for 12 h to remove all water.

2.4 Preparation of MXene/PPy@NiO Ternary Composite

NiO was deposited onto the MXene/PPy matrix using a hydrothermal route followed by calcination via a reported method with slight modifications [17]. Typically, 100 mg MXene/PPy was suspended in 40 mL of 0.05 M $Ni(NO_3)_2{\cdot}6H_2O$ solution after sonication for 30 min. For hydrothermal treatment, the resulting dispersion was enclosed within a 50 mL PTFE-lined autoclave and heated at a temperature of 120 °C for a duration of 12 h to promote uniform nucleation of nickel precursor species on the MXene/PPy surface, while minimizing the unnecessary oxidation of the MXene framework, facilitating the uniform nucleation of nickel precursor species on the surface coated with PPy, and preserving the structural integrity of the conductive PPy matrix. Upon cooling, the solid was rinsed thoroughly with deionized water and oven-dried at 80 °C for a

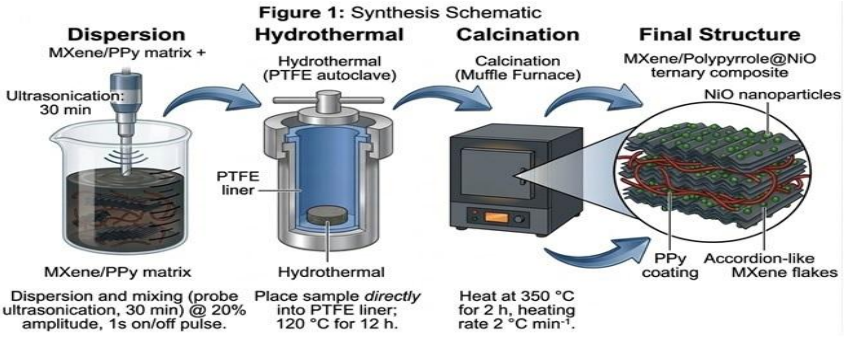

Figure 1: Synthesis Schematic

duration of 6 h. The resulting dry powder was calcined at 350 °C for 2 h directly to obtain NiO nanoparticles from the nickel precursor, yielding MXene/PPy@NiO composite.

Fig. 1: Synthesis of MXene/PPy@NiO ternary composite via ultrasonication, hydrothermal treatment at 120 °C for 12 h, and calcination at 350 °C, yielding NiO nanoparticles within an accordion-like MXene coated with PPy.

2.5 Electrode Fabrication

The synthesized MXene/PPy@NiO ternary nanocomposite was used to prepare working electrode materials [18]. In particular, an 8:1:1mass ratio of MXene/PPy@NiO/polymer binder (acetylene black (ACB)) was mixed, and N-methyl-2-pyrrolidone (NMP) was slowly added to obtain a uniform paste. The prepared slurry was coated onto the nickel foil current collectors with an area of 1 cm^2 and then vacuum-dried overnight (24 h) at 120 °C. The active material was loaded onto the electrodes at a mass of approximately 1.8 ± 0.1 mg cm^{-2}, and the thickness of the electrode was 50–60 μm, as measured using a micrometer. Only the mass of the electrochemically active materials was used to report the electrochemical parameters, in accordance with standard supercapacitor test protocols.

2.6. Characterization

The presence of surface functional groups of MXene, PPy, and NiO was confirmed by Fourier-transform infrared (FTIR) spectroscopy. Powder X-ray diffraction (XRD) was used to monitor the phase purity and crystalline structure and changes after formation. Field emission scanning electron microscopy (FESEM) and energy-dispersive X-ray spectroscopy (EDS) were used to examine the composite's morphology and elemental distribution. In addition, specific surface area, pore diameter, and total pore volume were obtained from N_2 adsorption-desorption isotherms (77 K) using the Brunauer–Emmett–Teller (BET) and BJH methods, respectively. To avoid changing the PPy structure and to remove nitrogen physically adsorbed on the sample, the samples were degassed under vacuum for 12 h at 60 °C before nitrogen adsorption measurements.

2.7. Determination of Electrode Potential Window

The stable operating voltage regions of the three-electrode system and MXene/PPy@NiO//YP50 asymmetric supercapacitor (ASC) were first identified in 1 M KOH aqueous electrolyte solution. The potential window of the working electrode in the three-electrode configuration was determined by preliminary cyclic voltammetry (CV) tests with Ag/AgCl reference electrode. The stable operating potential range of 0 to 0.6 V vs Ag/AgCl was chosen for the following three-electrode CV, galvanostatic charge–discharge (GCD), electrochemical impedance spectroscopy (EIS), and cycling experiments. The stable cell-voltage window was not measured independently in both the positive and negative electrodes, but rather the assembly of the ASC was measured, and a cell-voltage window from 0–1.6 V was chosen for two-electrode testing [19,20].

2.8 Electrochemical Measurements

The electrochemical testing was performed at room temperature in 1 M KOH using a three-electrode configuration with a working electrode of MXene/PPy@NiO, a reference electrode of Ag/AgCl, and a counter electrode of platinum foil. The same IR-drop correction was used for all analyses, and after 2000 cycles of GCD, cycling stability was evaluated. All measurements were done on three different independently prepared electrodes and expressed as mean ± SD [21]. Specific capacitance, energy density, and power density were determined by Equations (1-3). All three-electrode electrochemical measurements were recorded and reported with respect to the Ag/AgCl reference electrode. No potential conversion to the Standard Hydrogen Electrode (SHE) scale was applied to the reported three-electrode CV and GCD data. The Nyquist plots were processed to obtain the solution resistance (Rs), charge-transfer resistance (Rct), and qualitative ion-diffusion behavior in the high-frequency and low-frequency regions [22]. Specific capacitance with respect to the area under the CV curve was obtained by cyclic voltammetry and calculated from the curve using Equation 2.

$$Cs = I \times \frac{\Delta t}{m \times \Delta V} \quad \textbf{1}$$

$$Cs = \frac{\int_{V_1}^{V_2} I(V)\, dV}{mv\Delta V} \quad \textbf{2}$$

$$E = 0.5 \times Cs \times \frac{\Delta V^2}{3.6}\ (Wh\ kg^{-1}) \quad \textbf{3}$$

$$P = E \times \frac{3600}{\Delta t} \ (W\ kg^{-1}) \quad \textbf{4}$$

Consistent with standard supercapacitor evaluation protocols, where m is the mass of the electrochemically active material deposited on the current collector (excluding the conductive additive and polymer binder). All measurements were baseline corrected, and the area under each CV curve was numerically integrated.

2.9 Fabrication of MXene/PPy@NiO//AC Asymmetric Supercapacitor Device

The feasibility of MXene/PPy@NiO was assessed by assembling an asymmetric supercapacitor (ASC) with a cathode made of MXene/PPy@NiO and an anode made of YP50 activated carbon (AC), which were fabricated as described in Section 2.5. The mass ratio (m^+/m^-) was calculated based on the charge balance principle ($q^+ = q^-$), and the active mass loading of the positive and negative electrodes was optimized. The optimized active mass loadings were 1.8mg/cm² (MXene/PPy@NiO cathode) and 3.2mg/cm² (YP50 activated carbon anode) before assembling the asymmetric device [23].

$$\frac{m^+}{m^-} = \frac{C^- \times \Delta V^-}{C^+ \times \Delta V^+} \quad \textbf{5}$$

The operating cell-voltage window of 0–1.6 V was selected based on the electrochemical stability windows established independently for the positive and negative electrodes in 1 M KOH before device assembly. The charge-balanced electrode configuration (Eq. 5) allowed the full-cell testing without operating any of the electrodes beyond their stable ranges. The device capacitance (C), the specific energy (E), and the power density (P) were calculated according to Equations (5, 6, and 7), in which all the quantities were calculated with the total active mass of both electrodes, and the power density was obtained by taking the IR-corrected value as the operating voltage.

$$C_{device} = I \times \frac{\Delta t}{M \times \Delta V} \quad \textbf{6}$$

$$E = 0.5 \times C_{device} \times \frac{\Delta V^2}{3.6} \ (Wh\ kg^{-1}) \quad \textbf{7}$$

$$P = E \times \frac{3600}{\Delta t} \ (W\ kg^{-1}) \quad \textbf{8}$$

The total mass of electrochemically active materials in both electrodes (MXene/PPy@NiO and activated carbon) is denoted as M. The weights of the current collectors, binder, conductive additive, separator, and electrolyte were not included in the calculations because this is the standard practice for reporting asymmetric supercapacitors.

3. Results and Discussion

3.1. Physicochemical and Microstructure Analysis

A comprehensive physicochemical and microstructural characterization was performed to confirm the synthesis of the MXene/PPy@NiO ternary composite and to understand the structural features responsible for its electrochemical performance. FTIR spectroscopy was employed to identify successful incorporation of MXene, PPy, and NiO in the ternary nanocomposite, as shown in Fig. 2. The MXene/PPy sample demonstrated a broad band at 3440 cm^{-1}, which denotes the–OH asymmetric stretching, attributed to chemically bound water molecules and ambient surface moisture chemisorbed onto the high-energy active centers of the metal oxide nanoparticles [24]. The relative contributions of the −OH and −O terminations can, however, not be distinguished by FTIR, and the material is referred to as $Ti_3C_2T_x$ MXene throughout this work. The N-H stretching vibration of PPy appeared in the 3400-3200 cm^{-1} range. The characteristic stretching vibrations of C=C and C=N bonds of the conjugated PPy backbone were observed in the 1600-1450 cm^{-1} region, while C-N stretching and C-H bending appeared in the 1350-1250 cm^{-1} and 1100-900 cm^{-1} ranges, respectively [25]. Ti-O related vibrations appeared in the 1000-600 cm^{-1} region, supporting the presence of oxygenated MXene surface terminations [26]. Characteristic Ni–O vibrations were observed for NiO below 700 cm^{-1}. The presence of these characteristic bands in the spectrum of MXene/PPy proves that NiO has been integrated into the structure of MXene/PPy without affecting the basic structure of the individual components. The FTIR results provide further evidence of the presence of the characteristic functional groups of $Ti_3C_2T_x$ MXene, PPy, and NiO in the ternary composite. The small peak shifts and changes in peak intensity indicate that there are some interactions between the components at the interface, but definitive evidence for chemical bonding would need to be provided by other complementary techniques, like XPS. Hence, the FTIR analysis data are consistent with XRD, SEM, EDX, and electrochemical analysis data, which confirms the successful formation of the MXene/PPy@NiO composite.

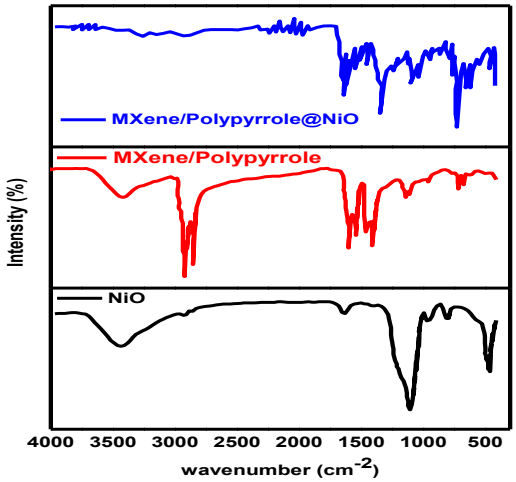

Fig. 2: FTIR spectra of MXene/PPy@NiO, MXene/PPy, and NiO

PXRD analysis was used to evaluate phase formation and structural evolution during ternary-composite formation. Figure 3 shows the PXRD patterns of MXene/PPy and MXene/PPy@NiO together with the corresponding reference diffraction data. The XRD pattern revealed that the (002) diffraction peak was shifted, and the intensity of the characteristic MAX-phase diffraction peaks was decreased, which proved that the hydrothermal conditions were optimal for the formation of the layered $Ti_3C_2T_x$ MXene. The presence of PPy may contribute broad and weak diffraction features because of its partially amorphous/conjugated polymer nature [27]. The MXene/PPy@NiO PXRD pattern demonstrates the successful deposition of NiO onto the MXene/ PPy matrix, as revealed by the presence of additional diffraction peaks with enhanced intensities relative to MXene/PPy and the presence of low-angle features related to MXene. The shift of the diffraction peak (002) towards lower diffraction angles after hybrid formation indicates a moderate increase in the interlayer spacing; the result implies that the accessibility of the electrolytes in the MXenes was partially suppressed, indicating partial resistance to MXene restacking, and that there was an increase in interlayer spacing after the hybrid formation [28]. While the XRD data indicate partial suppression of restacking, this is not evidence of complete exfoliation of the layered structure. The sharp decrease in the intensity of the characteristic MAX-phase reflections and the shift of the (002) diffraction peak show that a considerable amount of Al layers can be removed and that a layered $Ti_3C_2T_x$-type MXene product has been formed during the alkaline hydrothermal process. The diffraction data therefore agree with FTIR results and confirm that the synthesized

material contains both layered conductive domains and redox-active NiO crystallites. The peak shift and intensity changes for the observed phases confirm the formation of MXenes; however, the complete disappearance of the residual MAX phase can only be confirmed with further structural characterization.

Table 1: Structural Characterization

Sample	MXene d-spacing (Å)	D_{NiO} (nm)	S_{BET} (m^2 g^{-1})	Vpore (cm^3 g^{-1})	Average NiO Particle Size (nm)
MXene	14.5	-	55	0.35	-
MXene/PPy	15.2	-	60	0.42	-
MXene/PPy@NiO	15.5	12–15	74.28	0.54	14 ± 2

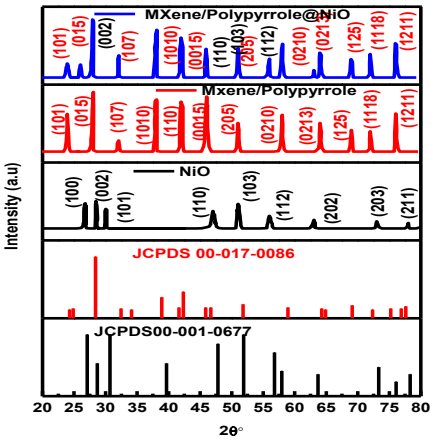

Fig. 3: PXRD patterns of MXene/PPy@NiO, MXene/PPy, and NiO. The reference diffraction pattern shown at the bottom corresponds to the standard ICDD/JCPDS card used for phase identification of NiO.

SEM images (Figure 4) show the morphology of NiO, MXene/PPy, and MXene/PPy@NiO. The pristine MXene-based sample exhibited a sheet-like wrinkled morphology typical of delaminated two-dimensional MXene structures coated with a conducting polymer. The PPy coating is found to connect neighbouring MXene sheets, which helps to increase the interlayer separation and the formation of a more open conductive network. Following hydrothermal deposition and calcination, the MXene/PPy@NiO composite developed a rougher and more hierarchical surface morphology due to the homogeneous dispersion of NiO NPs across the MXene/PPy framework [29,30]. Based on the SEM evidence, the proposed roles for each component are as follows: MXene acts as a two-dimensional conductive support, PPy reduces the degree of MXene restacking, and NiO supplies faradaic surface sites. The combination of the structural evidence, however, means that exfoliation is not complete, but only partial suppression of MXene restacking and improved electrolyte accessibility is suggested. The rough layered morphology (observed here, but not confirmed by cross-sectional HRTEM) and the higher BET surface area and larger XRD interlayer spacing are all consistent with partial suppression of MXene restacking after hybridization.

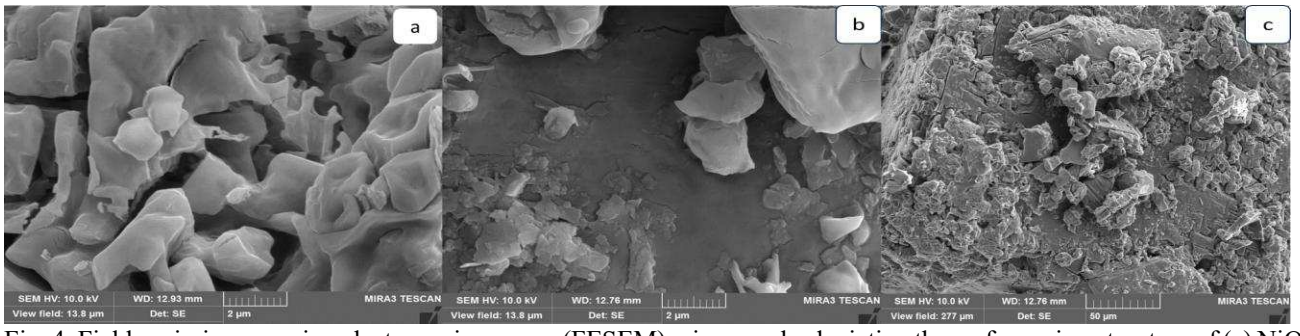

Fig. 4: Field-emission scanning electron microscopy (FESEM) micrographs depicting the surface microstructure of (a) NiO, (b) MXene/PPy, and (c) MXene/PPy@NiO composite.

EDX analysis confirmed the elemental composition of the synthesized samples. Figure 5 shows the EDX spectrum and elemental mapping of MXene/PPy@NiO. The MXene-containing samples showed Ti and C signals associated with the Ti_3C_2-based framework. The presence of N in MXene/PPy and MXene/PPy@NiO supports the successful incorporation of polypyrrole [31]. The ternary composite also showed Ni and O signals, confirming the presence of nickel oxide [32]. The simultaneous detection of Ti, C, N, Ni, and O in MXene/PPy@NiO demonstrates that all three targeted components are present in the final material.

Table 2: Quantitative elemental analysis of the synthesized materials (EDX)

Sample	Ti (at%)	C (at%)	N (at%)	Ni (at%)	O (at%)
MXene	22	36	-	-	12
MXene/PPy	21	35	8	-	13
MXene/PPy@NiO	21	35	8	22	14

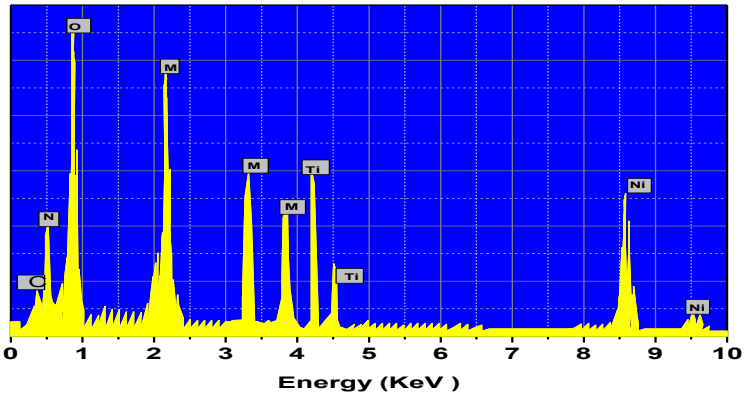

Fig. 5: EDX spectrum and elemental mapping of MXene/PPy@NiO.

The textural properties of the MXene/PPy@NiO composite were investigated based on N2 adsorption-desorption isotherms and the corresponding Barrett-Joyner-Halenda (BJH) pore-size distribution (PSD) as shown in Figures 6a and 6b. Specific

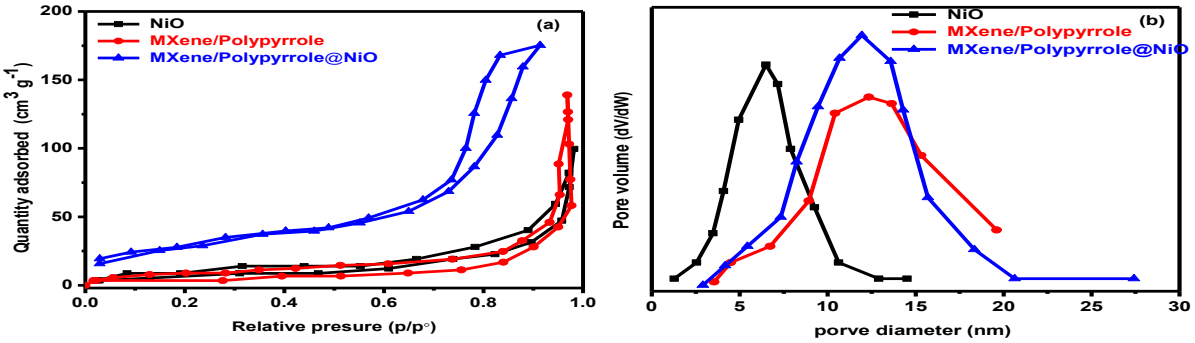

surface area and total pore volume of the ternary composite were 74.28 $m2g^{-1}$ (BET) and 0.54 cm^3g^{-1} (BET), respectively. The surface area is significantly improved compared to the conventional multilayer $Ti_3C_2T_x$ MXene, and this effect is explained by the presence of uniform NiO nanoparticles and the presence of PPy chains, which act as effective structural spacers with a partial hindrance to restacking of MXene and expose new electrochemically accessible surfaces. The process of hybridization does not completely exfoliate the material, but creates an open layered structure that has better electrolyte access. The hierarchical pore network is shown in the BJH pore-size distribution, where both micropores (~2 nm) and mesopores (approximately 2–4 nm) are present, ensuring a large number of active sites for charge storage and promoting electrolyte transport in the electrode [33]. Its highly interconnected mesoporous structure allows for a high diffusion rate of hydrated K^+ and OH^- ions throughout the electrode and a high number of electrochemically active sites and micropores for charge storage. These structural features work together to decrease ion diffusion lengths, increase electrolyte accessibility, and increase the amount of electrochemically active material utilized, consistent with the enhanced electrochemical performance of the MXene/PPy@NiO electrode.

(a) (b)

Fig. 6: (a) The Nitrogen adsorption and desorption isotherm of the MXene/PPy@NiO composite, (b) BJH pore-size distribution of the MXene/PPy@NiO composite.

4. Electrochemical Performance

4.1. Cyclic Voltammetry

The electrochemical measurements were carried out within the optimized operating potential windows established in Section 2.7, namely 0–0.6 V vs Ag/AgCl for the three-electrode configuration and 0–1.6 V for the assembled MXene/PPy@NiO//YP50 asymmetric supercapacitor (ASC). The performance of both the positive MXene/PPy@NiO electrode and the activated carbon negative electrode was optimized, respectively, before the assembly of the asymmetric device (Section 2.9). The final cell voltage (0-1.6 V) was chosen to allow for reversible cell operation during electrochemical measurements. Figure 7 shows the cyclic voltammograms of the pristine NiO, MXene/PPy, and MXene/PPy@NiO samples at a scan rate of 5 mV s^{-1}. The CV area enclosed by the ternary MXene/PPy@NiO electrode is the greatest, signifying better capacity retention due to the synergistic effect of the conductive MXene sheets, pseudocapacitive PPy, and redox-active NiO nanoparticles. The electrodes shown here showed broad anodic and cathodic redox features within the potential window that was investigated, as opposed to an ideal electric double-layer capacitor (EDLC), which normally has a rectangular voltammogram; this suggests that the electric double-layer and faradaic charge-storage processes are both present. The observed redox response is mainly attributed to the reversible transition between Ni^{2+} and Ni^{3+} in NiO and PPy, which also provides charge storage via reversible doping/dedoping processes. At the same time, PPy provided extra charge storage by reversible doping/dedoping behaviors, along with a conductive spacer to alleviate partial restacking of the MXenes and help electrons to access the electrolyte [34]. To examine the differences caused by the diffusion limitations and polarization effects, CVs were recorded at scan rates of 5 to 20 mV s^{-1}, and it was seen that the enclosed area gradually decreased as the scan rate increased, but the overall features were similar. This behaviour indicates for the ternary architecture the excellent electrochemical reversibility and ion-transport kinetics. The decreasing areas of the enclosed CVs with increasing scan rate found in the present study support the assumption that surface-controlled capacitive processes and diffusion-assisted faradaic reaction processes are occurring simultaneously, as experienced with the present hybrid electrode of MXene/PPy@NiO, as detailed in the following equation: $i = k_1v + k_2v^{1/2}$. Specific capacitance derived from integrated CV curves was 421 F g^{-1} at the scan rate of 5 mV s^{-1} and decreased gradually with increasing scan rate (Table 2), which is considered to be the diffusion limitations of the pseudocapacitive redox process. The specific capacitance obtained from the CV was determined by using Equation (2). The values derived from the CV are reported as specific capacitance (F g^{-1}), which is a common practice for hybrid pseudocapacitive electrodes with mixed capacitive and battery-type charge storage.

Table 3: Specific capacitance calculated from CV curves

Scan rate (mV s^{-1})	Specific capacitance (F g^{-1})	Capacitance retention (%)
5	421	100
10	382	90.7
20	338	80.3

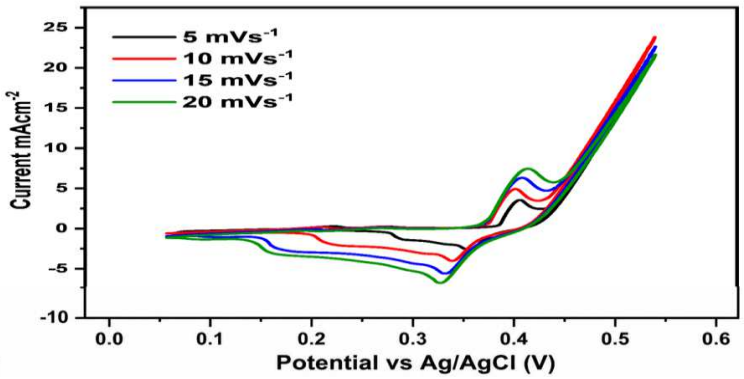

Fig. 7: CV curves of MXene/PPy@NiO recorded at scan rates of 5–20 mV s^{-1} within the optimized potential window of 0–0.6 V vs Ag/AgCl is used to calculate the CV-derived specific capacitance using Eq. (2).

4.2. Galvanostatic Charge-Discharge Analysis

Galvanostatic charge-discharge (GCD) measurements were also performed to examine the charge-storage capabilities of fabricated electrodes. The GCD profiles of pristine NiO, MXene/PPy, and MXene/PPy@NiO at the same current density are shown in Figure 8a. The measurements have been performed in the optimized potential window between 0–0.6 V vs Ag/AgCl with no electrolyte decomposition during charge-discharge cycling. In comparison with all electrodes, the MXene/PPy@NiO had the longest discharge time, demonstrating its excellent charge storage capacity. The synergistic effect of the highly conductive MXene framework, the pseudocapacitive PPy network, and the reversible Ni^{2+}/Ni^{3+} redox reactions of NiO, all of which promote rapid electron transport and efficient electrolyte-ion diffusion, results in the improved electrochemical response. The GCD curves obtained with different current densities are shown in Figure 8b. The discharge time gradually decreased with increasing current density (1 to 10 A g^{-1}) due to decreased ion diffusion time and polarization; the charge-discharge profile was well preserved, and good rate capability was obtained. As expected for hybrid pseudocapacitive electrodes, the specific capacitance of the MXene/PPy@NiO electrode decreased with increasing current density, reaching 517 F g^{-1} at 1 A g^{-1} before levelling off at lower current densities. This reduction can be explained by the growing polarization/diffusion limitations at high currents, where the utilization of electroactive sites will be less with the fast charge/discharge cycle. The GCD curves also show an initial IR drop that is relatively small but still noticeable, showing relatively low solution resistance, which is consistent with the relatively low solution resistance measured by EIS, followed by a relatively straight discharge curve with slight curvature characteristic of reversible faradaic reactions with a small deviation from ideal triangular symmetry, showing the presence of electric double-layer capacitance and reversible faradaic reactions. The discharge curve is not typical of an ideal triangular EDLC response, nor is it typical of a battery-type plateau, but rather a hybrid charge-storage mechanism of MXene, PPy, and NiO. The observed behaviour is typical of MXene/conducting polymer/transition-metal oxide hybrid electrodes, where the surface-controlled capacitive processes occur in parallel with diffusion-assisted redox processes. GCD (517 F g^{-1}) and CV (421 F g^{-1} at 5 mV s^{-1}) calculated capacitances are greater than the previous values. This difference is due to different principles of calculation, which are used for these two electrochemical techniques. The active material will be able to utilize a much higher percentage of the reversible faradaic reaction during discharge; capacitance will be more sensitive to the presence of polarization and diffusion limitations depending on the scan rate when using CV-derived capacitance. The same kind of difference has been previously widely reported in hybrid pseudocapacitive electrode materials.

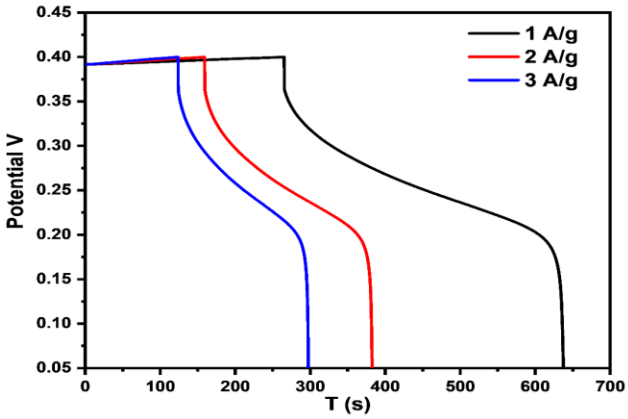

Fig. 8: (a) The MXene/PPy@NiO has been designed using GCD curves and related specific capacitance.

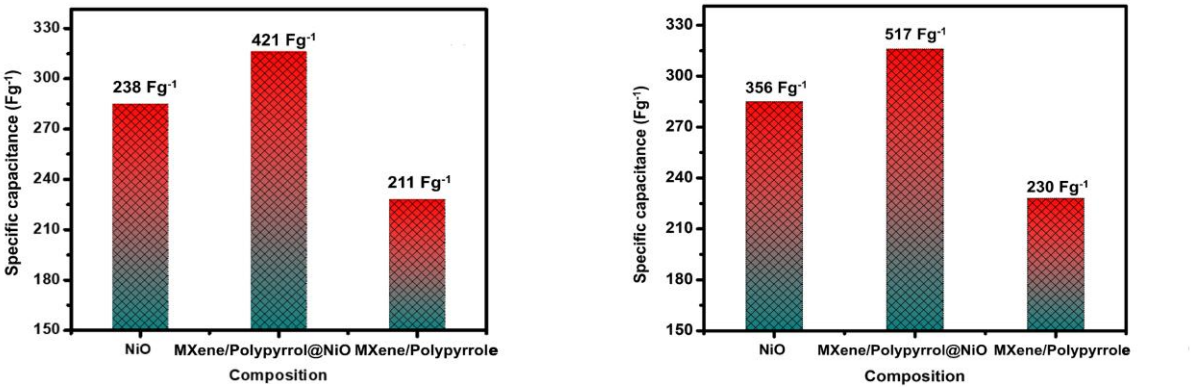

(b) (c)

Fig. 8: Comparative specific capacitance histograms of pristine NiO, MXene/PPy, and MXene/PPy@NiO electrodes derived from (b) cyclic voltammetry (CV) at a scan rate of 5 mV s^{-1} and (c) galvanostatic charge–discharge (GCD) at a current density of 1 A g^{-1}.

4.3. Energy and Power Density Output Evaluation

The simply designed MXene/PPy@NiO//YP50 asymmetric supercapacitor (ASC) was tested in a two-electrode configuration within a cell-voltage window of 0–1.6 V. The Ragone plot is a summary of the electrochemical performance of the assembled ASC (Figure 9). At 180 F g^{-1}, specific capacitance was attained with a current density of 1 A g^{-1}, which results in a maximum specific energy density of 64 Wh kg^{-1} at a maximum specific power density of 640 W kg^{-1}. The specific energy density was also reduced to 42 Wh kg^{-1} when operated at a higher power density of 2000 W kg^{-1}. As such, the Ragone plot clearly shows the inverse relationship between energy density and power density, showing that the device maintains a significant portion of its energy-storage capacity when run at the higher power. This drop in SED with an increase in SPD is related to the shorter discharge time and increased polarization at higher current densities. The observed drop in energy density from 64 Wh kg^{-1} to 42 Wh kg^{-1} with the increase in power density from 640 to 2000 Wh kg-1 accordingly demonstrates the typical energy–power trade-off of asymmetric supercapacitors. The device-level performance observed is due to the complementary charge storage properties of both electrodes. The activated-carbon negative electrode mainly gives rise to the electric double-layer capacitance, while the MXene/PPy@NiO positive electrode is responsible for conductive pathways and pseudocapacitive and faradaic charge storage of PPy and NiO. These mechanisms make the ASC able to function on top of a 1.6 V cell-voltage window with reasonable energy output at high power demands.

Table 4: Electrochemical Performance Comparison

Electrode Material	Specific Capacitance (F g^{-1})	Energy density (Wh kg^{-1})	Power density (W kg^{-1})	Cycling Stability (%)	Reference
NiO	250	30	1000	70	This work
MXene/PPy	380	50	1200	78	This work

Three-electrode MXene/PPy@NiO	517 (electrode)	25.85 (electrode)	1000	82% after 2000 cycles	This work
Two-electrode ASC (MXene/PPy@NiO//YP50)	180 (device)	64.0 (device)	640	88% after 5000 cycles	This work
Mxene pseudocapacitor ($Ti_3C_2T_x$)	442.9	34.5	624	92% after 3000 cycles	[37]

The assembled ASC also exhibited good device-level cycling stability, retaining 88% of its initial capacitance after 5000 charge–discharge cycles, as discussed in detail in Section 4.6. Self-discharge and leakage-current characteristics were not investigated in the present study and should therefore be considered in future device-level investigations.

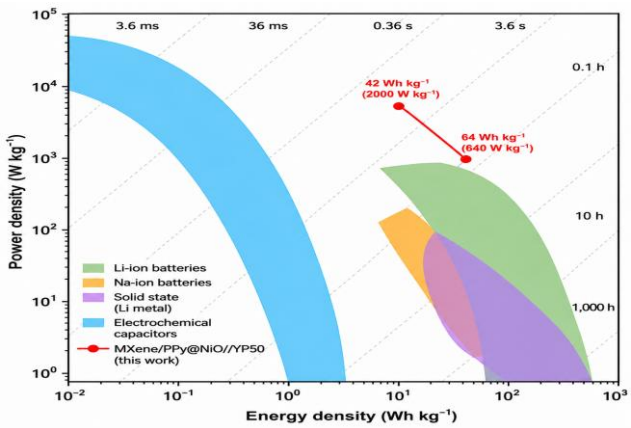

Fig. 9: Ragone plot of the MXene/PPy@NiO//YP50 asymmetric supercapacitor showing the relationship between specific energy density and specific power density obtained from galvanostatic charge–discharge measurements. Device-level values were calculated using the combined active mass of the positive and negative electrodes.

4.4. Electrochemical Impedance Spectroscopy

The fabricated electrodes were studied to understand their charge-transfer behavior and ion-transport characteristics by electrochemical impedance spectroscopy (EIS). The Nyquist plots together with the fitted equivalent circuit model are presented in Figure 10. The intercepts in the high-frequency region of all the electrodes were small and were related to the solution resistance, Rs, and the charge-transfer resistance, Rct, at the electrode/electrolyte interface, which was followed by a depressed semicircle. The fitted circuit was made up of solution resistance (Rs), charge-transfer resistance (Rct), a constant phase element (CPE), and a Warburg diffusion element (W), and resulted in a good qualitative description of the circuit's response. The Warburg linear section in the low-frequency region corresponds to the behavior of electrolyte ion transport. MXene/PPy@NiO showed the lowest charge-transfer resistance of ~1.8 Ω (from equivalent-circuit fitting), based on the smallest semicircle diameter among the investigated electrodes, indicating the fastest interfacial electron-transfer kinetics between the two. The low-frequency line slope further highlights improved electrolyte access and reduced ion-diffusion resistance, which may be related to the porous structure of PPy/NiO and the conductive MXene framework. The relatively small IR drop in the GCD curves lends credence to this, which indicates that charge transport is efficient from the surface all the way to the interior of the composite electrode. As a whole, the outcomes demonstrated that the ternary structure does indeed improve the electron conduction and electrolyte-ion diffusion, resulting in improved electrochemical performance [38].

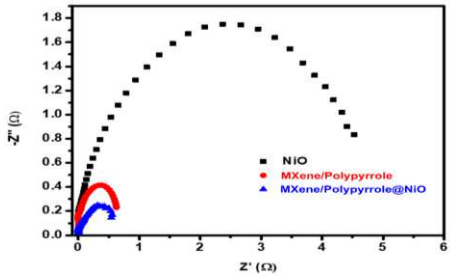

Fig. 10: Nyquist plots and fitted equivalent circuit of the NiO, MXene/PPy, and MXene/PPy@NiO.

4.5. Double-Layer Capacitance and Electrochemically Active Surface Area

The electrochemically accessible surface area (ECSA) of NiO, MXene/PPy, and MXene/PPy@NiO electrodes was estimated using non-Faradaic double-layer capacitance (Cdl) measurement, as shown in Figure 11. The electrochemically accessible surface area (ECSA) of NiO, MXene/PPy, and MXene/PPy@NiO was compared using the double-layer capacitance measurement. However, NiO showed a relatively low value of Cdl because its conductivity was comparatively low and particles were aggregated, thus reducing access to the active surface sites. However, the introduction of MXene/PPy led to improved Cdl as the surface area of the MXene network and the conductive polymer matrix were accessible, and the effective ion transport pathways were provided [39]. Overall, the best Cdl value the electrode exhibited was 0.925 mF cm-2 for the ternary MXene/PPy@NiO electrode. This means that it has the maximum surface area available for the electrochemically accessible surface area of the samples tested. This observation is in good agreement with the BET and SEM analyses, which indicated a hierarchical porous structure with higher surface roughness and better accessibility to the electrolyte.

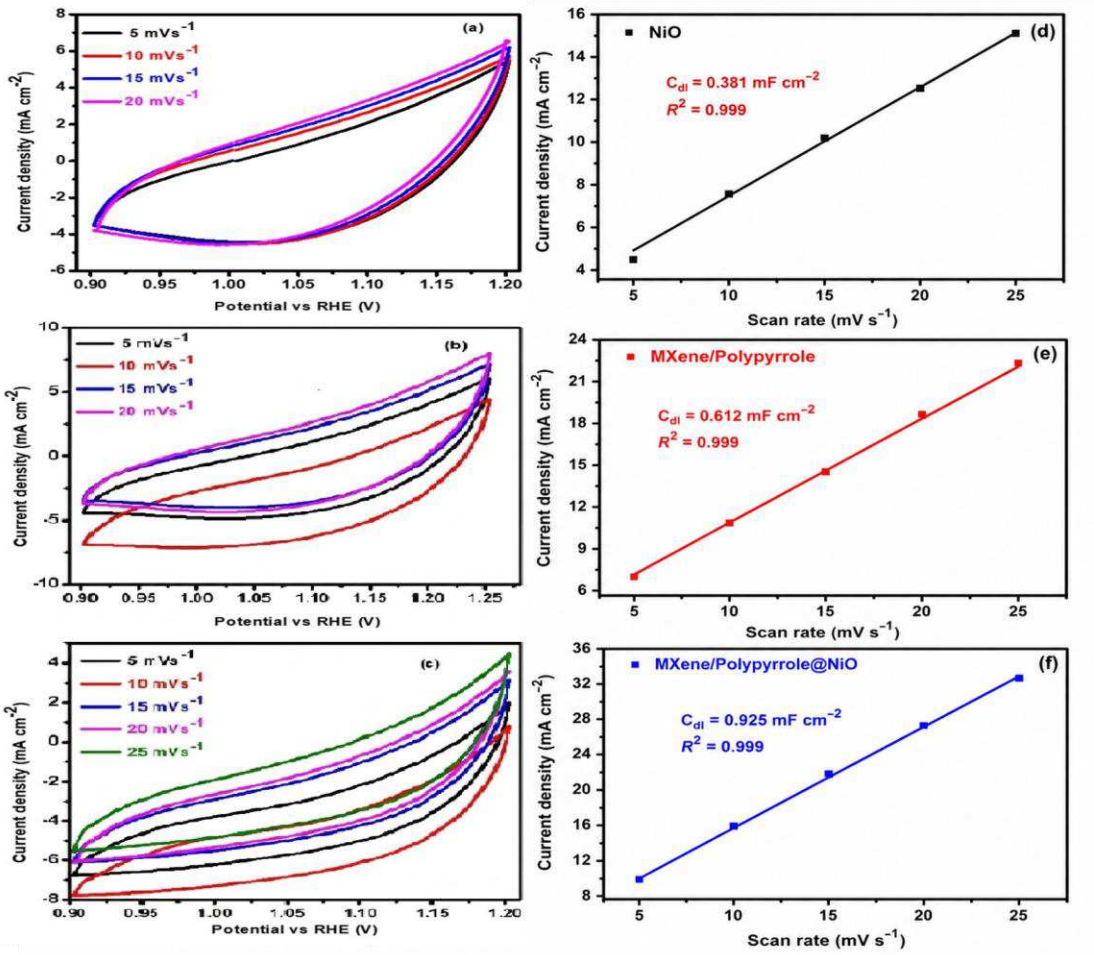

Fig.11: Cyclic voltammograms recorded in the non-faradaic potential region at different scan rates for (a) NiO, (b) MXene/PPy, and (c) MXene/PPy@NiO together with the corresponding linear regression plots used to determine the double-layer capacitance (Cdl): (d) NiO, (e) MXene/PPy, and (f) MXene/PPy@NiO.

4.6. Cycling Stability

One of the criteria that is key to assessing the long-term electrochemical performance of supercapacitor electrodes is their cycling stability, especially when the electrodes are hybrid ones, such as conducting polymers and transition-metal oxides. To investigate the cycling performance of the MXene/PPy@NiO electrode, the electrode was repeatedly subjected to galvanostatic charge-discharge cycling, as shown in Figure 12. The electrode exhibited good electrochemical stability in terms of capacitance under repeated charge/discharge cycles, with 82% of the capacitance remaining after 2000 cycles. This structural reorganization, partial swelling/shrinking of PPy during repeated doping/dedoping processes, and continuous

faradaic reactions of NiO can be the source of the progressive decrease of capacitance. However, the excellent conducting MXene framework and porous hybrid structure provide excellent electron transport, as well as good electrolyte accessibility during long cycles, resulting in a small degradation of overall performance [40]. The capacitance loss was not significant, and the Coulombic efficiency was above 99% during the whole cycling period, which shows high reversibility of charge-discharge reactions. The above-mentioned capacitance retention of the assembled ASC device (88% after 5000 cycles) is not to be interpreted as an intrinsic property of the materials, but rather as a result of the different electrochemical environment of the two-electrode and three-electrode testing setups.

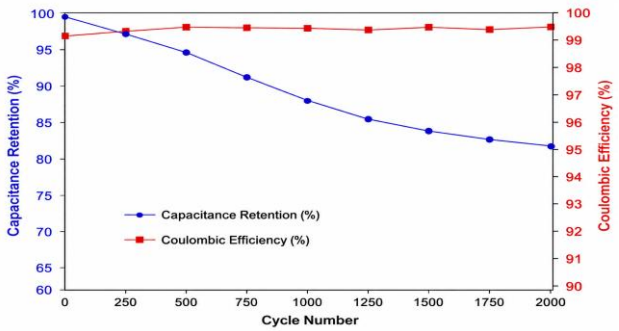

Fig. 12: Cycling stability of the MXene/PPy@NiO electrode measured by repeated galvanostatic charge–discharge cycling. Capacitance retention (%) and Coulombic efficiency (%) are plotted as a function of cycle number for 2000 cycles in 1 M KOH electrolyte.

4.7. Practical Device Demonstration

The electrochemical performance of the assembled MXene/PPy@NiO//YP50 asymmetric supercapacitor (ASC) was investigated in a two-electrode configuration using an optimized cell-voltage window of 0–1.6 V, established from the stable potential windows of the individual positive and negative electrodes before device assembly. As shown in Figure 13, two ASC devices connected in series successfully illuminated a commercial red LED, demonstrating the ability of the fabricated device to store and deliver electrical energy under a simple laboratory demonstration. This result provides a qualitative demonstration of the device's practical output capability; however, LED illumination alone does not establish application-level performance.

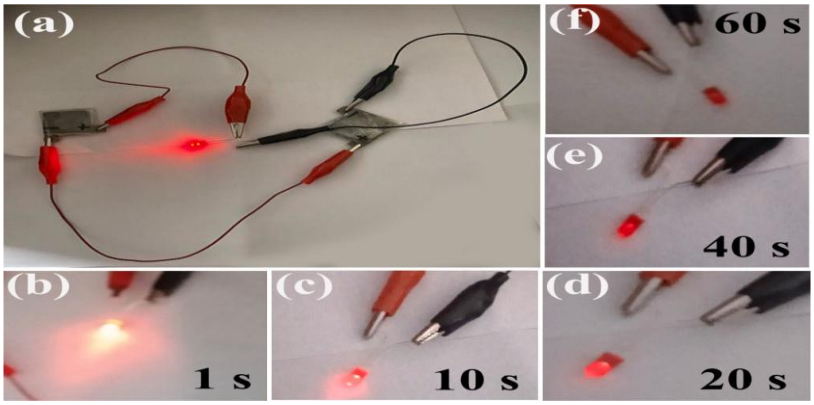

Fig. 13: Practical demonstration of the MXene/PPy@NiO//YP50 asymmetric supercapacitor (ASC). Two identical MXene/PPy@NiO//YP50 ASC devices connected in series successfully powered a commercial red LED, demonstrating practical energy-storage capability.

5. Proposed Charge-Storage Mechanism

The complementary functions of MXene, PPy, and NiO make the composite films MXene/PPy@NiO have enhanced electrochemical properties. MXene is a highly conductive two-dimensional framework that offers electron-transport pathways and electric double-layer and limited surface intercalation charge storage, as shown in Figure 14. PPy contributes to reducing MXene restacking, increasing structural flexibility, and adding pseudocapacitance due to reversible polymer doping/dedoping. NiO contributes to reversible faradaic charge-storage reactions occurring in an alkaline medium through the Ni^{2+}/Ni^{3+} transition.

$$NiO + OH^- \leftrightarrow NiOOH + e^-$$

The hierarchical porous structure increases electrolyte penetration and reduces ion diffusion distances throughout the electrode. Concentrated coexistence of microporous and mesoporous domains provides more electrochemically accessible active sites and also allows for rapid electrolyte-ion transport. Meanwhile, the MXene/PPy conductive network reduces charge-transfer resistance and improves utilization of NiO redox sites. Overall, charge storage originates from three complementary mechanisms: electric double-layer charge accumulation from MXene, polymer faradaic pseudocapacitance from PPy, and NiO faradaic redox activity [41]. This combined mechanism explains the high specific capacitance, low R_{ct}, increased C_{dl}, and improved energy-power response of the ternary composite.

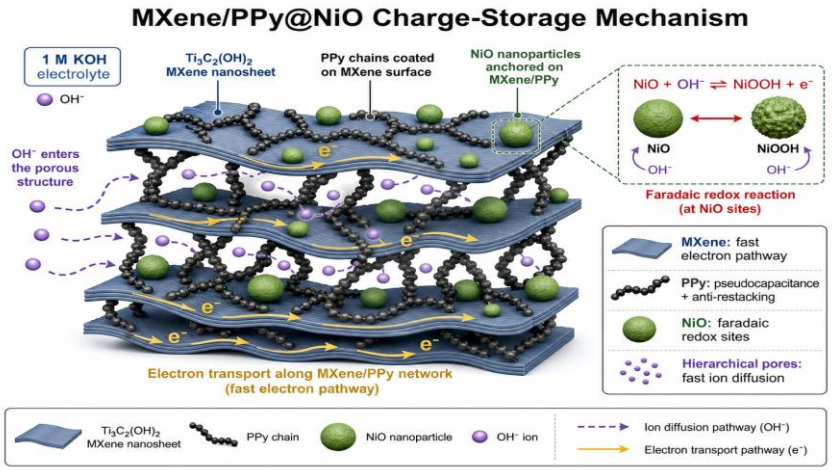

Fig. 14: Schematic illustration of the charge-storage mechanism in MXene/PPy@NiO.

6. Conclusion

By combining conductive MXene sheets, pseudocapacitive polypyrrole, and redox-active NiO nanoparticles, a $Ti_3C_2T_x$ MXene/Polypyrrole@NiO ternary nanocomposite was successfully developed through a fluoride-free hydrothermal synthesis strategy as a high-performance supercapacitor electrode. FTIR, PXRD, SEM, EDX, and BET analyses were used to verify the successful synthesis of a hierarchical composite featuring a porous structure and an electrochemically accessible surface area. The combination of MXene, PPy, and NiO yielded a synergistic effect in terms of enhanced electrochemical performance, with possible improvements in electrical conductivity, ion transport, and the number of redox sites. Galvanostatic charge-discharge (GCD) and cyclic voltammetry (CV) were used to obtain specific capacitances of 517 F g^{-1} at 1 A g^{-1} in 1 M KOH aqueous electrolyte and 421 F g^{-1} at a scan rate of 5 mV s^{-1}, respectively. The electrochemical resistance (Rct) measured by electrochemical impedance spectroscopy was 1.8Ω, which is low. The double-layer capacitance analysis revealed that the C_{dl} value (0.925mF cm^{-2}) was the highest of the electrodes investigated, which corresponds to a large electrochemically active surface area. The electrode of MXene/PPy@NiO exhibited 82% capacitance retention after 2000 charge/discharge cycles, indicating its good electrochemical stability. In addition, the fabricated MXene/PPy@NiO//YP50 asymmetric supercapacitor exhibited a specific capacitance of 180 F g^{-1}, a maximum energy density of 64 Wh kg^{-1} at the corresponding power density of 640 W kg^{-1}, and retained 88% of its initial capacitance after 5000 charge–discharge cycles. The efficient lighting of a commercial LED red module also shows the potential for a practical energy-storage capability of the assembled device. In summary, the results show that rational interface engineering is a promising approach to the development of advanced electrode materials that combine MXene, conducting polymers, and transition-metal oxides for high-performance supercapacitor applications.

References

1. Dong, Z., Tao, Y., Lai, S., Wang, T., & Zhang, Z. (2025). Powering future advancements and applications of battery energy storage systems across different scales. *Energy Storage and Applications*, *2*(1), 1. https://doi.org/10.3390/esa2010001
2. Abraham, T. R., Sunil, K., Shah, M., Ashok, N., & Thomas, S. (2023). Energy storage devices: batteries and supercapacitors. In *IWA Publishing eBooks* (pp. 61–84). https://doi.org/10.2166/9781789063592_0061
3. Wu, J., Ju, Z., Zhang, X., Marschilok, A. C., Takeuchi, K. J., Wang, H., Takeuchi, E. S., & Yu, G. (2022). Gradient design for High-Energy and High-Power batteries. *Advanced Materials*, *34*(29), e2202780. https://doi.org/10.1002/adma.202202780
4. Dutta, A., Mitra, S., Basak, M., & Banerjee, T. (2022). A comprehensive review on batteries and supercapacitors: Development and challenges since their inception. *Energy Storage*, *5*(1). https://doi.org/10.1002/est2.339
5. Pameté, E., Köps, L., Kreth, F. A., Pohlmann, S., Varzi, A., Brousse, T., Balducci, A., & Presser, V. (2023). The many deaths of supercapacitors: degradation, aging, and performance fading. *Advanced Energy Materials*, *13*(29). https://doi.org/10.1002/aenm.202301008
6. Fusco, L., Gazzi, A., Shuck, C. E., Orecchioni, M., Alberti, D., et al., (2022). Immune profiling and multiplexed Label-Free detection of 2D MXEnes by mass cytometry and High-Dimensional imaging. *Advanced Materials*, *34*(45), e2205154. https://doi.org/10.1002/adma.202205154
7. Al-Harthi, E. A., Ali, M. K. M., Imran, M., Aljameel, A. I., Ansari, A., Ahmed, S., Shinde, S. M., & Arif, M. (2026). Review: Design strategies and developments in Ti3C2Tx MXene composites for advanced supercapacitor applications. *Journal of Materials Science*, *61*(13), 8331–8364. https://doi.org/10.1007/s10853-026-12348-0
8. Chen, Y., Yu, B., & Peng, L. (2023). Two-dimensional MXENE Nanomaterials: Preparation, Structure Modulation, and the Applications in Electrochemical Energy Storage. *Recent Patents on Nanotechnology*, *18*(2), 92–116. https://doi.org/10.2174/1872210517666230427161120
9. Fei, L., Lei, L., Xu, H., Guo, X., Chen, B., Han, X., Chen, X., Huang, Q., & Wang, D. (2025). Ion transport behaviors in MXenes for electrochemical energy storage and conversion. *Carbon Energy*, *7*(3). https://doi.org/10.1002/cey2.678
10. Zia, J., & Tejaswini, M. S. S. R. (2025). Advancements in binary and ternary transition-metal-based composites for high-performance supercapacitors: a comprehensive review. *RSC Advances*, *15*(12), 9055–9080. https://doi.org/10.1039/d5ra00528k
11. Pramanik, A., Sengupta, S., Saju, S. K., Chattopadhyay, S., Kundu, M., & Ajayan, P. M. (2024). Ternary metal sulfides as electrode materials for Na/K-ion batteries and electrochemical supercapacitors: advances/challenges and prospects. *Advanced Energy Materials*, *14*(36). https://doi.org/10.1002/aenm.202401657
12. Wei, F. (2023). Figures and Data for the Nature Protocols：Solution-based self-assembly of two-dimensional ordered mesoporous conducting polymer sheets with tunable properties. *Figshare*. https://doi.org/10.6084/m9.figshare.22550017
13. Jaiswal, S., Soni, V., Singh, P., & Gupta, A. (2024). Role of cation deficiency and the inductive effect in Ti-Doped NIO for developing superior electrocatalysts for the oxygen evolution reaction. *ACS Applied Energy Materials*, *7*(19), 8814–8825. https://doi.org/10.1021/acsaem.4c01774
14. Arulanantham, R. R., & Ragupathi, V. (2025). Insights into the electrochemical performance of NiO/MXene anodes for lithium-ion batteries. *Journal of Solid-State Electrochemistry*, *30*(2), 567–577. https://doi.org/10.1007/s10008-025-06417-8
15. Ezika, A. C., Sadiku, E. R., Ray, S. S., Hamam, Y., Folorunso, O., & Adekoya, G. J. (2022). Emerging advancements in Polypyrrole MXENE hybrid nanoarchitectonics for capacitive energy storage applications. *Journal of Inorganic and Organometallic Polymers and Materials*, *32*(5), 1521–1540. https://doi.org/10.1007/s10904-022-02280-6
16. Chaudhary, V., Kaushik, A., Furukawa, H., & Khosla, A. (2022). Review—Towards 5th Generation AI and IoT-driven sustainable intelligent sensors based on 2D MXENES and Borophene. *ECS Sensors Plus*, *1*(1), 013601. https://doi.org/10.1149/2754-2726/ac5ac6
17. Adekoya, G. J., Adekoya, O. C., Sadiku, R. E., Hamam, Y., & Ray, S. S. (2022). Applications of MXENE-Containing Polypyrrole Nanocomposites in electrochemical energy storage and conversion. *ACS Omega*, *7*(44), 39498–39519. https://doi.org/10.1021/acsomega.2c02706
18. Vattikuti, S. V. P., Shim, J., Rosaiah, P., Mauger, A., & Julien, C. M. (2023). Recent advances and strategies in mxene-based electrodes for supercapacitors: applications, challenges, and future prospects. *Nanomaterials*, *14*(1), 62. https://doi.org/10.3390/nano14010062

19. Liang, W., & Zhitomirsky, I. (2022). MXene-polypyrrole electrodes for asymmetric supercapacitors. *Electrochimica Acta*, *406*, 139843. https://doi.org/10.1016/j.electacta.2022.139843
20. Sheraz, S., Niaz, N. A., Shakoor, A., & Hussain, F. (2026). Electrochemical energy storage applications of MXene/PPy composites. *Journal of Materials Science Materials in Electronics*, *37*(12). https://doi.org/10.1007/s10854-026-17270-4
21. Perdana, M. Y., Johan, B. A., Abdallah, M., Hossain, M. E., Aziz, M. A., Baroud, T. N., & Drmosh, Q. A. (2024). Understanding the behavior of supercapacitor materials via electrochemical impedance spectroscopy: A review. *The Chemical Record*, *24*(5), e202400007. https://doi.org/10.1002/tcr.202400007
22. Zhang, Y., Li, X., Li, Z., & Yang, F. (2024). Evaluation of electrochemical performance of supercapacitors from equivalent circuits through cyclic voltammetry and galvanostatic charge/discharge. *Journal of Energy Storage*, *86*, 111122. https://doi.org/10.1016/j.est.2024.111122
23. Luanwuthi, S., Thaemwan, T., Suebsing, N., Sasrimuang, S., Iamprasertkun, P., Puchongkawarin, C., Sawangphruk, M., & Jaiboon, O. (2026). Current collector selection for aqueous sodium-ion energy storage: Corrosion considerations in Water-in-Salt Electrolytes. *SSRN Electronic Journal*. https://doi.org/10.2139/ssrn.6506550
24. Mohamad, N. a. R. C., Lee, H., Gong, M., Ye, C., Bu, Y., Lin, Z., Won, D., Kim, J., Mota, F. M., & Kim, D. H. (2025). Modulating oxygen evolution reaction pathways via (Oxy)Hydroxide-Driven surface reconstruction on Ti_3C_2 MXene electrocatalysts. *Small*, *21*(40), e08259. https://doi.org/10.1002/smll.202508259
25. Jing, L., Zhuo, K., Sun, L., Zhang, N., Su, X., Chen, Y., Hu, X., Feng, R., & Wang, J. (2024). The mass-balancing between positive and negative electrodes for optimizing energy density of supercapacitors. *Journal of the American Chemical Society*, *146*(21), 14369–14385. https://doi.org/10.1021/jacs.4c00486
26. Lei, Y., Ding, M., Wu, H., Yin, D., Li, Y., Jiang, B., Sun, K., Zhang, Y., & Du, H. (2022). A broadband and strong microwave absorption of $Ti_3C_2T_x$ MXene/PPy composites with a core-shell structure. *Synthetic Metals*, *293*, 117254. https://doi.org/10.1016/j.synthmet.2022.117254
27. Huang, B., Tong, X., Zhang, X., Feng, Q., Rumyantseva, M. N., Prakash, J., & Li, X. (2023). MXene/NiO composites for chemiresistive-type room-temperature formaldehyde sensor. *Chemosensors*, *11*(4), 258. https://doi.org/10.3390/chemosensors11040258
28. Sugunan, A., Rethnakumaran, A. V., Radhakrishnan, A. B., & Menamparambath, M. M. (2026). Interfacial polymerization-induced engineering of $Ti_3C_2T_x$/PPy with Cu functionalization for electrochemical uric acid sensing. *ACS Applied Nano Materials*, *9*(23), 10654–10667. https://doi.org/10.1021/acsanm.6c00975
29. Vishaka, E., Dharshini, M. P., Shally, V., & Jayam, S. G. (2022). NiO-CdO nanocomposite for photocatalytic applications. *Materials Today Proceedings*, *68*, 294–298. https://doi.org/10.1016/j.matpr.2022.05.180
30. Shen, H., Wang, J., Huang, H., Ji, J., & Li, L. (2024). Polymorphic Polypyrrole-Modified MXene nanosheets for broadband microwave absorption. *ACS Applied Nano Materials*, *7*(11), 13089–13100. https://doi.org/10.1021/acsanm.4c01549
31. Singh, A., Goyal, V., Singh, J., Kaur, H., Kumar, S., Batoo, K. M., Gaur, J., Pal, M., Rawat, M., & Hussain, S. (2022). Structurally and morphologically engineered single-pot biogenic synthesis of NiO nanoparticles with enhanced photocatalytic and antimicrobial activities. *Journal of Cleaner Production*, *343*, 131026. https://doi.org/10.1016/j.jclepro.2022.131026
32. Batool, F., Miran, W., Ahmed, M., Rizwan, S., Naeem, O., Zaheer, H., & Liaqat, U. (2025). Impact of polypyrrole/MXene modified anode on bioelectricity generation in microbial fuel cells. *Journal of Applied Electrochemistry*, *55*(7), 1925–1935. https://doi.org/10.1007/s10800-025-02275-4
33. N, S., & Mahalakshmi, S. (2024). A study on the oxidative property using thermogravimetric analysis of NiO nanoparticles prepared by a simple wet chemical method. *Chemical Physics Impact*, *8*, 100613. https://doi.org/10.1016/j.chphi.2024.100613
34. Osman, M., Karim, M. R., Hassan, H., Hakami, A., H-e, M. M. S., Iqbal, M., & Mumtaz, S. (2025). "Optimized electrochemical performance and longevity in asymmetric supercapacitors using binder-free MOF-808/Ti_2N electrodes." *Journal of Energy Storage*, *122*, 116682. https://doi.org/10.1016/j.est.2025.116682
35. Saraswathi, K., Reddy, M. S. B., Jayarambabu, N., Harish, C., Rao, K. V., & Rao, T. V. (2024). NiO embedded PANI /TI_3C_2T MXene detector for electrochemical enzyme-free glucose detection. *Surfaces and Interfaces*, *56*, 105728. https://doi.org/10.1016/j.surfin.2024.105728

36. Kadam, S. A., Kadam, K. P., & Pradhan, N. R. (2024). Advancements in 2D MXene-based supercapacitor electrodes: synthesis, mechanisms, electronic structure engineering, flexible wearable energy storage for real-world applications, and future prospects. *Journal of Materials Chemistry A*, *12*(29), 17992–18046. https://doi.org/10.1039/d4ta00328d
37. Wei, Y., Kumar, K. D., Zhang, L., & Li, J. (2025). Pseudocapacitive materials for energy storage: properties, mechanisms, and applications in supercapacitors and batteries. *Frontiers in Chemistry*, *13*, 1636683. https://doi.org/10.3389/fchem.2025.1636683
38. Xue, C., Wu, T., Zhao, W., Wei, Y., Lv, K., Li, X., Yan, W., Li, X., & Hao, X. (2024). High-rate electrochemical supercapacitor with attractive energy density assembled from infused Undaria pinnatifida-based activated carbon. *Journal of Energy Storage*, *80*, 110362. https://doi.org/10.1016/j.est.2023.110362
39. Ahmad, M., Shuja, A., Murtaza, I., Fahad, S., & Khan, M. S. (2025). Synergistic Integration of MXenes with Conducting Polymers to Enhance the Specific Capacitance of Asymmetric Supercapacitors. *Journal of Materials Science: Materials in Electronics*, *36*(18). https://doi.org/10.1007/s10854-025-15164-5
40. Hou, Z., Yang, Q., Lu, H., Li, Y., & Zhao, Q. (2025). Toward superior electrochemical capacitance with hierarchically nanostructured polypyrrole/MXene hybrid hydrogel modified by lignosulfonate. *ACS Omega*, *10*(27), 29476–29487. https://doi.org/10.1021/acsomega.5c02827
41. Bai, W., Li, C., Pan, F., Luo, Y., Gao, T., Yu, D., Wang, X., Sun, H., & Wang, S. (2024). High-stability supercapacitors based on MXene/Spherical g-PPy composite electrodes. *Electrochimica Acta*, *490*, 144300. https://doi.org/10.1016/j.electacta.2024.144300